coatings

MDPI

Article

Differences in Microstructure and Properties of 16 mm Thick 6082 Aluminum Alloy Under Different Heat Source Conditions

Zan Ju [1], Ruxu Huang [2], Xiaozhong Xie [2], Shu Liu [1], Feiyun Wang [1,*] and Juan Fu [1,*]

[1] School of Materials Science and Engineering, Jiangsu University of Science and Technology, Zhenjiang 212003, China
[2] China Ship Scientific Research Center, Wuxi 214082, China
* Correspondence: wangfeiyunmse@126.com (F.W.); fujuan@just.edu.cn (J.F.); Tel.: +86-15651883658 (F.W.); +86-13775365926 (J.F.)

Abstract

6082 aluminum alloy is widely applied in marine engineering, rail transportation and other industries owing to its excellent comprehensive performance. Welding heat source characteristics exert a decisive influence on the microstructure and mechanical properties of welded joints and become a major constraint for the application of medium-thick aluminum alloy welded structures. In this work, comparative tests of TIG and MIG welding were carried out on 16 mm thick 6082 aluminum alloy plates. Combining thermal simulation, metallographic observation and mechanical property tests, the temperature field distribution, microstructure, microhardness, tensile properties and bending properties of the two kinds of joints were systematically studied. The results show that TIG welding possesses high heat input, forming a broad temperature field with steep thermal gradients. Its weld microstructure is coarse and accompanied by severe coarsening of Mg_2Si precipitates, and the joint presents a highly fluctuating M-shaped microhardness distribution. The average tensile strength of TIG welded joints is 194 MPa, and all specimens fracture in the heat-affected zone. By contrast, MIG welding with low heat input produces a uniform temperature field, as well as a fine and homogeneous weld microstructure with dispersed precipitates. Its microhardness distribution is stable, and the average tensile strength reaches 256 MPa, 32% higher than that of TIG joints. Both welding methods deliver favorable bending performance. The difference in heat input and cooling behavior changes the grain evolution and precipitate characteristics and further dominates the final mechanical performance of joints. MIG welding is more suitable for multi-layer, multi-pass welding of 16 mm thick 6082 aluminum alloy. This work clarifies the correlation between heat input, microstructure and mechanical properties, and the optimized process can effectively improve the microstructural uniformity of the weld joint and enhance its mechanical properties.

Keywords: 6082 aluminum alloy; TIG welding; MIG welding; heat source characteristics; microstructure; mechanical properties

Check for updates

Academic Editor: Jaichan Lee

Received: 15 May 2026
Revised: 16 June 2026
Accepted: 19 June 2026
Published: 21 June 2026

Copyright: © 2026 by the authors. Licensee MDPI, Basel, Switzerland. This article is an open access article distributed under the terms and conditions of the Creative Commons Attribution (CC BY) license.

1. Introduction

Aluminum alloys feature low density, high specific strength, excellent corrosion resistance [1], superior thermal conductivity and good formability. Owing to these advantages, they have become essential structural materials for marine engineering, rail transportation, shipbuilding, aerospace and lightweight equipment [2]. As engineering components

develop toward larger size and lighter weight, the application of welded medium-thick aluminum alloy components has been continuously expanded. Nevertheless, welded joints often suffer from microstructural inhomogeneity and deteriorated mechanical properties, which adversely affect the long-term service safety of components [3]. Welding heat input strongly governs the solidified microstructure of welds, precipitate morphology and final mechanical performance of joints [4]. Grain coarsening, precipitate growth and joint softening induced by welding thermal cycles limit the widespread application of aluminum alloy welded structures [5,6]. Therefore, selecting appropriate welding methods and optimizing process parameters are critical to addressing the above challenges.

To meet the practical demands of aluminum alloy welding, a variety of welding technologies have been well developed. In addition to friction stir welding [7], laser welding [8], and ultrasonic welding [9], tungsten inert gas (TIG) welding and metal inert gas (MIG) welding, as the most widely used fusion welding methods, have become the mainstream processes for welding aluminum alloy structural components due to their stable welding processes, excellent weld quality, and high adaptability [10]. TIG welding uses a non-consumable tungsten electrode, and the welding process is performed in an inert gas atmosphere to shield the weld from the air. The weld bead exhibits excellent formation quality with no spatter, and the heat-affected zone is narrow, effectively reducing the occurrence of welding defects. It is well suited for welding non-ferrous metals such as aluminum and titanium alloys, as well as dissimilar metals. However, this method has low welding efficiency and, under conditions of high heat input, can easily lead to grain coarsening in the weld, thereby reducing the strengthening effect of the joint. MIG welding uses a consumable electrode wire, offering high welding efficiency and strong deposition capabilities. It is suitable for the efficient welding of thick aluminum alloy components, enabling stable molten pool stirring and promoting uniform weld metal microstructure. But the welding process is prone to spatter, and the prolonged exposure to high temperatures can lead to coarse grain structure in the weld and heat-affected zone. It also places high demands on the shielding gas, wire feed rate, and current stability, making it difficult to control the process parameters. The two welding processes differ substantially in heat input mode, heat source characteristics and molten pool behavior [11,12].

Meanwhile, with the increasing application of welded structures made of medium-thick aluminum alloy plates [13], multi-layer and multi-pass welding has been frequently adopted in the welding of thick components using conventional welding processes [14]. This further exacerbates heat accumulation during welding, which can easily lead to joint softening, increased deformation, and microstructural inhomogeneity, making it difficult to simultaneously meet the dual requirements of welding efficiency and joint performance. The fundamental differences between TIG and MIG welding in terms of heat input mode, heat source characteristics, and molten pool behavior directly result in significant differences in the grain evolution, precipitation behavior, and mechanical properties of the welded joints [15,16]. While existing research has primarily focused on comparative TIG and MIG welding tests on thin plates, significant gaps remain in studies of multi-layer, multi-pass welding conditions for 16 mm thick 6082 aluminum alloy. The current literature lacks characterization of heat source behavior based on finite element temperature field simulations, and a systematic correlation among heat source characteristics, microstructure and mechanical properties has not yet been established, making it difficult to guide the selection of welding processes for medium-thick plate components.

Based on the above analysis and actual industry needs, this paper systematically compares the heat source characteristics, heat input patterns, and welding process features of TIG welding and MIG welding in response to the application requirements of aluminum alloy welded structures. It investigates the macrostructure, microstructure,

hardness distribution, tensile properties, and bending properties under these two welding methods. It analyzes the influence of welding heat input on the grain structure, precipitation phase morphology, and mechanical properties of the joints, reveals the mechanisms of microstructural evolution and performance regulation in TIG and MIG welded joints, and clarifies the applicable ranges and directions for process optimization of the two welding processes, focusing specifically on 16 mm thick 6082 aluminum alloy multi-layer multi-pass welding under a fixed set of process parameters. This paper combines finite element thermal simulation with experimental measurements to detail a comprehensive simulation workflow, including the input of temperature-dependent thermophysical properties, node-based multi-pass weld path layout, double-ellipsoidal heat source calibration, boundary condition setup, and thermal cycle analysis. The present work fills the above-mentioned research gaps and ultimately provides a theoretical basis and technical support for the selection of welding processes, parameter optimization, and performance enhancement of medium-thick aluminum alloy welded structures.

2. Test Materials and Methods

2.1. Materials

The test base material consists of a 16 mm thick 6082-T6 aluminum alloy plate (Southwest Aluminum Co., Ltd., Chongqing, China), measuring 450 mm × 300 mm × 16 mm. The filler wire used for TIG welding is ESAB OK Tigrod5183 (ESAB, Gothenburg, Sweden), while the wire used for MIG welding is SAL5183 (Chuanwang Welding Materials Co., Ltd., Zhengzhou, China). The shielding gas for both processes is argon with a purity of 99.99%. The chemical compositions of the aluminum alloy base metal and welding wire, as well as the room-temperature mechanical properties of the aluminum alloy, are shown in Tables 1 and 2.

Table 1. Chemical composition of aluminum alloy base metal and welding wire (wt.%).

Materials	Si	Fe	Cu	Mn	Mg	Cr	Zn	Ti	Al
Base	0.7–1.3	0.5	0.10	0.4–1.0	0.6–1.2	0.25	0.20	0.10	Bal.
Tigord5183	<0.2	<0.2	/	0.6	4.8	/	/	/	Bal.
SAL5183	≤0.4	≤0.4	≤0.1	4.3–5.2	/	0.05–0.25	≤0.25	≤0.15	Bal.

Table 2. Mechanical properties of aluminum alloys at room temperature.

Material	R_m/MPa	$R_{p0.2}$/MPa	A(%)
6082 aluminum alloy	≥300	≥255	≥9

2.2. Welding Equipment and Tests

TIG welding uses a TIG welder manufactured by Ruide Thermal Equipment Co., Ltd. (Suzhou, China). This welder features three functions: shielded metal arc welding, DC TIG, and pulsed DC TIG. It is equipped with a water-cooling unit that allows connection to a water-cooled welding torch. The maximum welding current is 400 A, the maximum filler wire diameter is 5.5 mm, and the maximum tungsten electrode diameter is 3.2 mm. In this test, a 3.2 mm diameter cerium–tungsten electrode was selected, and AC power was used for welding. MIG welding uses welders manufactured by Kenbei Welding Technology Co., Ltd. (Wuxi, China), with a welding range of 20 A/12 V to 500 A/40 V. Figure 1 shows the principles of TIG and MIG. It can be seen that TIG welding uses a non-consumable tungsten electrode to generate an arc, requires separate wire feeding, and keeps the heat source separate from the filler metal. However, in MIG welding, the welding wire acts as the consumable electrode, performing both the functions of conducting electricity and

providing filler material, thereby integrating the heat source and the filler metal into a single unit.

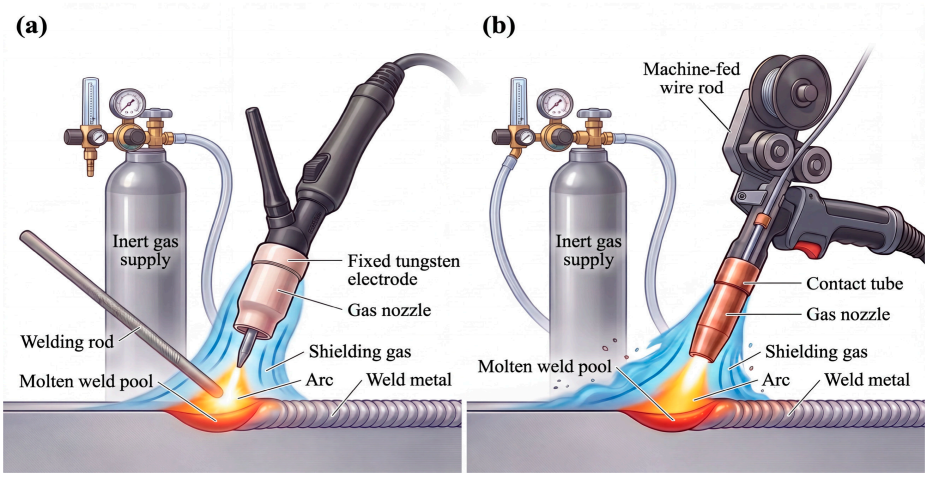


Figure 1. Principles of welding methods: (**a**) TIG; (**b**) MIG.

Figure 2 shows the groove type for the two welding methods. Both welding processes use a V-groove with a 60° angle and a 2 mm gap. Preheating is required prior to welding to reduce stress and strain in the test specimens.

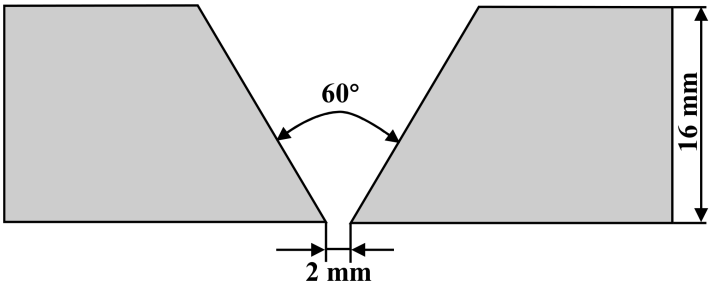


Figure 2. Schematic diagram of weld joint groove.

The welding heat input is expressed as:

$$E = \frac{\eta IU}{v} \quad (1)$$

$$v = \frac{L}{t} \quad (2)$$

In Equations (1) and (2), η is thermal efficiency coefficient. I, U, v, L and t are welding current, welding voltage, welding speed, welding length and welding time respectively. Set the value of η to 0.375 and L to 300 mm. The TIG and MIG welding process parameters are shown in Tables 3 and 4, respectively. The TIG process contains 9 welding passes while the MIG process has 10 passes. The difference in pass numbers is quite small, and the resulting cumulative thermal effect can be neglected. Therefore, this study mainly takes the average heat input per pass as the key index to compare the thermal characteristics of the two welding processes and their influences on the microstructure and properties of joints.

Table 3. TIG welding process test parameters.

Welding Process	Layer	Pass	Welding Current/A	Welding Voltage/V	Welding Time/s	Heat Input/(kJ/cm)	Total Welding Time/s	Average Heat Input/(kJ/cm)
TIG	1	1	330	31	115	14.70	959	13.48
	2	2	341	31	121	15.97		
	3	3	326	30	86	10.52		
		4	320	30	97	11.65		
	4	5	333	31	127	16.39		
		6	333	31	113	14.58		
	5	7	333	31	118	15.23		
		8	333	31	115	14.83		
		9	308	29	67	7.48		

Table 4. MIG welding process test parameters.

Welding Process	Layer	Pass	Welding Current/A	Welding Voltage/V	Welding Time/s	Heat Input/(kJ/cm)	Total Welding Time/s	Average Heat Input/(kJ/cm)
MIG	1	1	180	25	40	2.25	376	2.11
	2	2	190	23	40	2.23		
		3	190	23	40	2.23		
	3	4	180	25	40	2.25		
		5	180	25	36	2.03		
		6	180	25	36	2.03		
	4	7	180	25	36	2.03		
		8	180	25	36	2.03		
		9	180	25	36	2.03		
		10	180	25	36	2.03		

2.3. Analytical Test Methods

2.3.1. Microstructural Characterization

The cross-sections of the welded joint specimens were prepared using electric discharge machining. Use 180-grit sandpaper to remove wire-cutting marks from the surface, then pre-grind the surface with 400-, 800-, 1200-, 1500-, and 2000-grit sandpaper to ensure the specimen surface is smooth, with few and shallow scratches. Polishing was performed using a 0.05-μm SiO_2 suspension. After cleaning with alcohol, etch with Keller's reagent (4 mL HF + 2 mL HNO_3 + 6 mL HCl + 28 mL H_2O) for 10–15 s. Macroscopic and microscopic analyses of the joints were performed using a Zeiss Smartzoom 5 3D microscope (Zeiss, Oberkochen, Germany), and an inverted metallurgical microscope, respectively. Further microstructural characterization was carried out using a Hitachi Regulus 8100 scanning electron microscope (SEM) (Hitachi, Tokyo, Japan).

2.3.2. Mechanical Property Tests

A hardness test of the welded joints was performed using a German KB 30S (KB Prüftechnik GmbH, Hochdorf-Assenheim, Germany) fully automatic Vickers hardness tester with a load of 3 kg. The tensile test was conducted using a CMT5205 electronic universal testing machine (SUST, Zhuhai, China) at a loading rate of 2 mm/min. The bending test was conducted using a bending testing machine with a 40 mm diameter indenter and a bending angle of 90°. The specimen dimensions are shown in Figure 3.

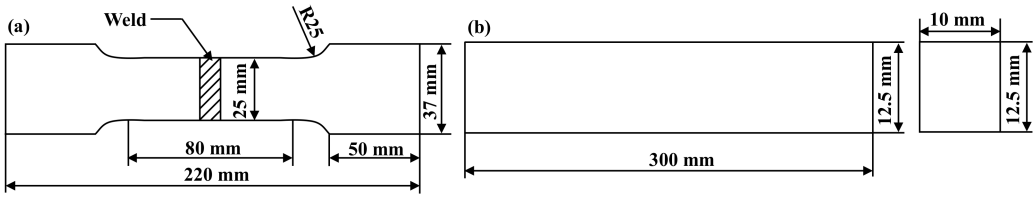


Figure 3. Schematic of specimen dimensions: (**a**) tensile specimen; (**b**) bending specimen.

2.4. Finite Element Model

Before performing welding process simulation, a three-dimensional geometric model must be created and meshed, as shown in Figure 4. A fine mesh is used near the high-temperature welding heat-affected zone, while a coarser mesh is used in areas farther from the heat-affected zone, with a 3:1 transition to reduce the number of mesh elements [17]. The thermophysical properties of 6082 aluminum alloy are shown in Table 5.

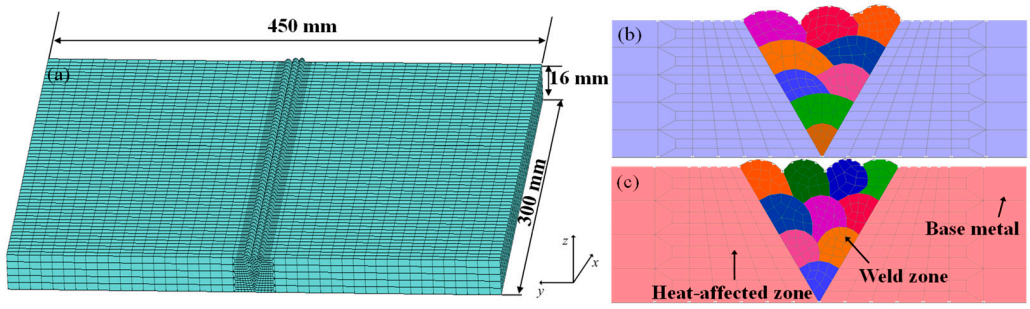


Figure 4. Meshing of the welding process: (**a**) overall mesh division; (**b**) mesh division in TIG welding; (**c**) mesh division in MIG welding.

Table 5. Thermophysical properties of 6082 aluminum alloy.

Temperature/°C	Mass Density/(kg/m^3)	Heat Conductivity/[W/(m·K)]	Specific Heat/[J/(kg·K)]	Thermal Expansion Coefficient/($\times 10^{-6}$K^{-1})
0	2702	182	882	23.2
20	2700	180	890	23.5
100	2692	176	915	23.8
200	2685	172	940	24.2
300	2678	168	960	24.5
400	2670	165	980	24.8
500	2662	161	1000	25.1
600	2640	152	1150	25.8
650	2620	145	1200	26.1

Welding paths are established to replicate the actual travel trajectory of the welding torch. As multi-layer and multi-pass welding is performed in this study, an independent path is assigned to each weld pass. All welding trajectories are straight lines with no complex curves, so the node-based method is utilized for path definition. The start and end points of the heat source are defined as the arc initiation and termination points in practical welding, forming the complete moving route. The arc is set perpendicular to the direction of heat source movement. The detailed configuration of welding paths is presented in Figure 5.

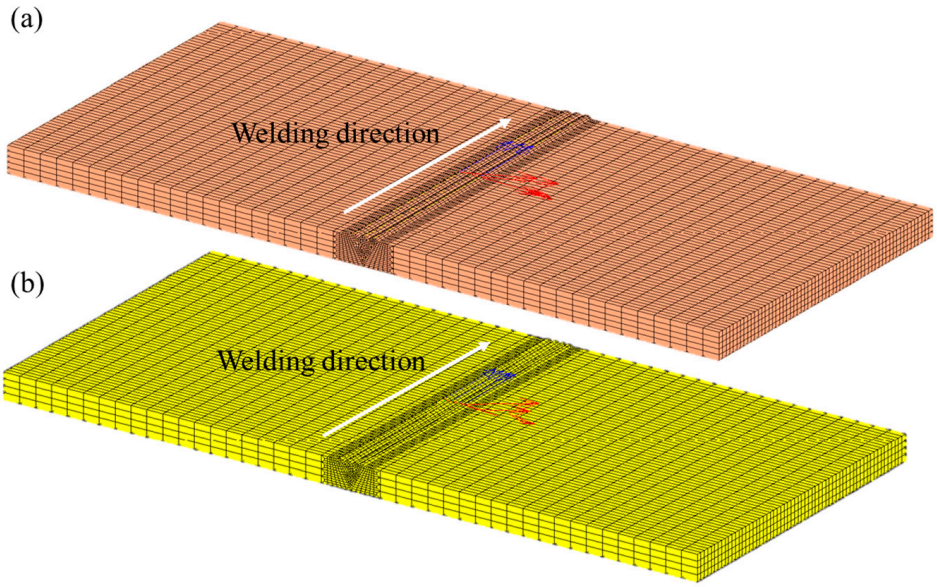


Figure 5. Setting results of welding path: (**a**) TIG; (**b**) MIG.

To simulate the welding process more realistically, this study adopted a double-ellipsoidal heat source model, as shown in Figure 6. The heat flux density is expressed as [18,19]:

$$q(x,y,z,t) = \frac{6\sqrt{3}f_f}{abc_1\pi\sqrt{\pi}}\exp\left(-3\left(\frac{x^2}{a^2}+\frac{y^2}{b^2}+\frac{(z-vt)^2}{{c_1}^2}\right)\right) \quad (3)$$

$$q(x,y,z,t) = \frac{6\sqrt{3}f_r}{abc_2\pi\sqrt{\pi}}\exp\left(-3\left(\frac{x^2}{a^2}+\frac{y^2}{b^2}+\frac{(z-vt)^2}{{c_2}^2}\right)\right) \quad (4)$$

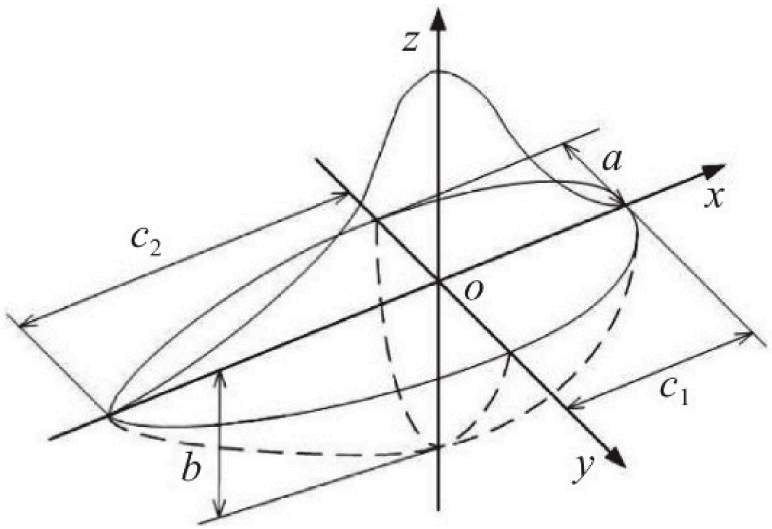


Figure 6. Double-ellipsoidal heat source model.

In Equations (3) and (4), f_f and f_r are heat flux distribution coefficients. $f_f + f_r = 2$, a, b, c_1, and c_2 are the geometric dimensions of the molten pool [18]. The values can be seen in Table 6. The units for a, b, c_1, and c_2 are all meters. The above parameters are determined based on the measured molten pool dimensions. The weld width, weld penetration and longitudinal extension length of the molten pool are obtained by metallographic observation. The semi-axis sizes of the heat source are initially set in accordance with the geometric proportions of the molten pool, so that the spatial shape of the heat source

matches the actual heating range of the electric arc. The energy distribution coefficients are selected according to the temperature distribution characteristics of the moving arc, which conforms to the rule that the temperature gradient is steeper at the front and gentler at the rear of the molten pool during welding.

Table 6. Heat source parameter values.

Parameter	Value
a	0.004
b	0.005
c_1	0.003
c_2	0.004
f_f	0.7
f_r	1.3

Before performing welding simulation calculations, the initial and boundary conditions must be defined. The initial conditions are used to determine the temperature of the workpiece prior to welding. Since all welding tests in this study were conducted indoors at room temperature, the initial temperature of the entire workpiece was uniformly set to 20 °C. Boundary conditions include convection at the weld interface and heat flux within the weld volume. A convective heat transfer boundary condition is applied to the entire outer surface of the model to simulate natural heat dissipation between the workpiece and the air. The arc heat source is modeled using volumetric heat flux, with the heat load applied only to the weld and the base metal region immediately adjacent to it. The results of the boundary condition definition are shown in Figure 7.

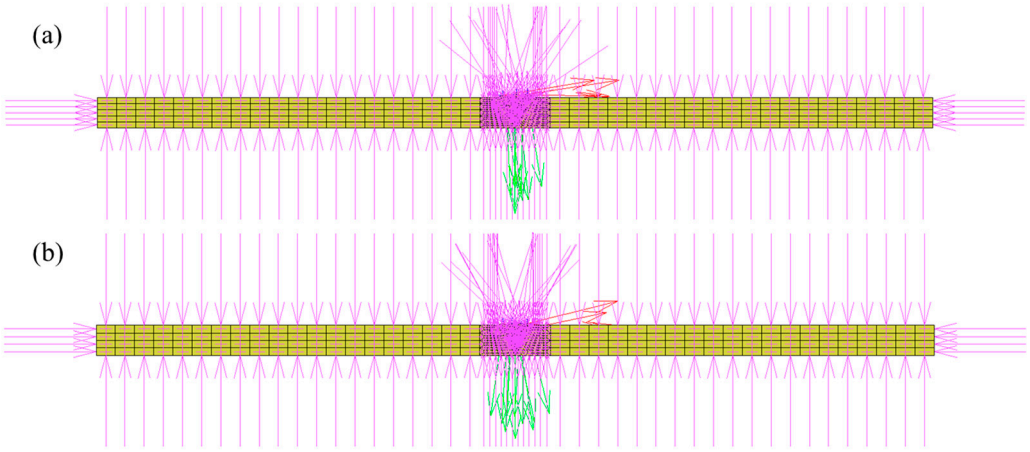


Figure 7. Setting results of boundary conditions: (**a**) TIG; (**b**) MIG.

Figure 8 shows a comparison of numerical simulations with experimental results for TIG and MIG welding. The upper limit for the temperature zone is set to 650 °C (the liquidus temperature of 6082 aluminum alloy). The gray area in the figure represents the simulated geometry of the molten pool [20]. The comparison of the numerical simulation results with experimental data indicates that the model ensures simulation accuracy and can serve as a basis for subsequent temperature field simulations of 16 mm thick 6082 aluminum alloy.

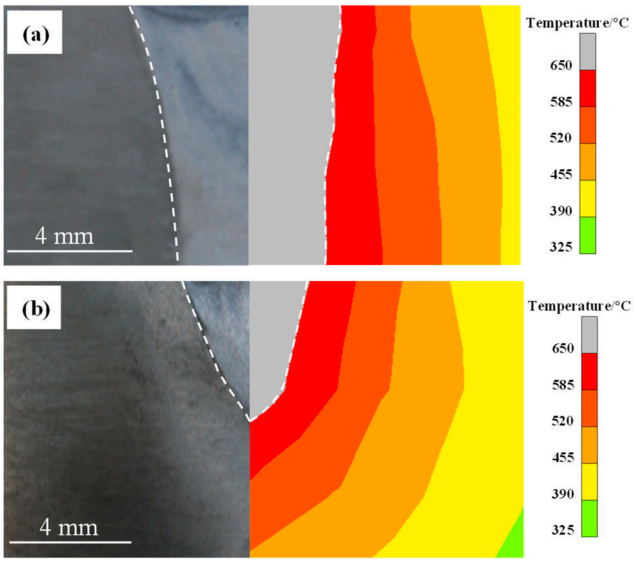


Figure 8. Comparison between simulated result and experimental result: (**a**) TIG; (**b**) MIG.

3. Results and Discussion

3.1. Temperature Distribution and Thermal Cycle

Figure 9 shows the temperature distribution during the two welding processes. It is clearly evident that a temperature peak occurs at the center of the molten pool, with the temperature gradually decreasing outward from the center. The temperature gradient distribution indicates temperature variations at different locations within the molten pool [21]. The spacing between isotherms at the front end of the molten pool is much smaller than at the rear end, implying that the temperature gradient at the front end is greater than at the rear end. Figure 9a,d show the overall temperature distribution. A comparison of the overall temperature fields for TIG welding and MIG welding reveals that the temperature field for TIG welding covers a wider area. In contrast, the temperature field for MIG welding is confined to an extremely narrow region immediately adjacent to the weld.

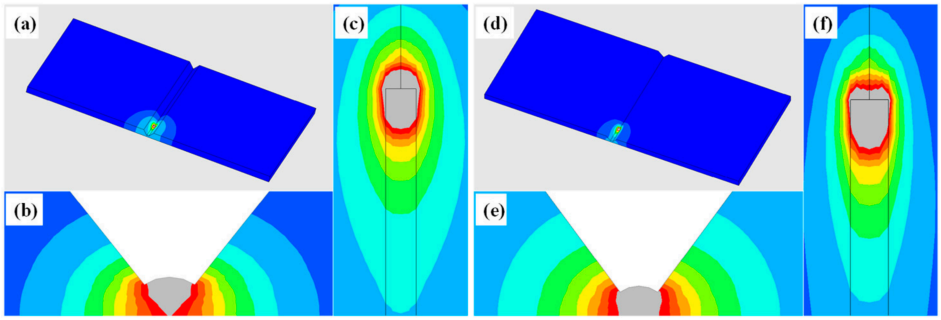


Figure 9. Temperature distributions: (**a**) overall temperature distribution in TIG welding; (**b**) cross-sectional temperature distribution in TIG welding; (**c**) top view of temperature distribution in TIG welding; (**d**) overall temperature distribution in MIG welding; (**e**) cross-sectional temperature distribution in MIG welding; (**f**) top view of temperature distribution in MIG welding.

Figure 9b,e show the cross-sectional temperature distributions during two welding processes. As shown in the figure, TIG welding has high heat input, relatively concentrated energy, and a steep temperature gradient. In contrast, MIG welding has low heat input, relatively dispersed energy, and a gentle temperature gradient. Figure 9c,f show top views of the temperature field distributions, both of which exhibit the characteristic double-

ellipsoidal distribution typical of a moving heat source. Such distributions are consistent with the double-ellipsoidal heat source model shown in Figure 6.

Figure 10 shows the thermal cycle curves for the two welding methods at different nodes. Under identical incremental step settings in finite element analysis, the duration of high-temperature retention within a single calculation increment is essentially consistent for TIG and MIG. However, the actual total welding time for the TIG specimen is longer than that for MIG, with an average single-pass welding time of 106.6 s for TIG and 37.6 s for MIG. This leads to a longer overall high-temperature residence time for the TIG joint and a correspondingly lower average cooling rate during the cooling stage. The analysis shows that the peak temperature at the start of TIG welding can reach 1350–1400 °C, while subsequent passes stabilize at 800–1000 °C. The heat input is high, the heat accumulation effect is significant, and the cooling rate is slow. In contrast, the peak temperature at the start of MIG welding is approximately 1050–1100 °C. In subsequent passes, the peak temperature rapidly drops to 300–400 °C. This process features low heat input, minimal heat accumulation, and rapid cooling. The difference in thermal cycling between the two processes essentially stems from differences in heat transfer mechanisms. TIG welding is a non-consumable electrode arc welding process in which the heat is applied directly to the base metal, resulting in high heat input. MIG welding, or metal inert gas welding, primarily uses heat to melt the filler wire, resulting in low heat input to the base metal. When comparing temperatures in different areas of a weld, taking the first pass as an example, the peak temperatures in the weld zone (nodes TIG-2 and MIG-2) are significantly higher than those in the heat-affected zone (nodes TIG-3 and MIG-3) and the base metal (nodes TIG-4 and MIG-4). The welding arc acts as a concentrated, moving heat source, directing energy directly into the weld pool and making the weld the hottest area. Heat diffuses into the base metal on both sides through thermal conduction, and the temperature decreases exponentially with distance. Consequently, the temperatures in the heat-affected zone and the base metal decrease sequentially.

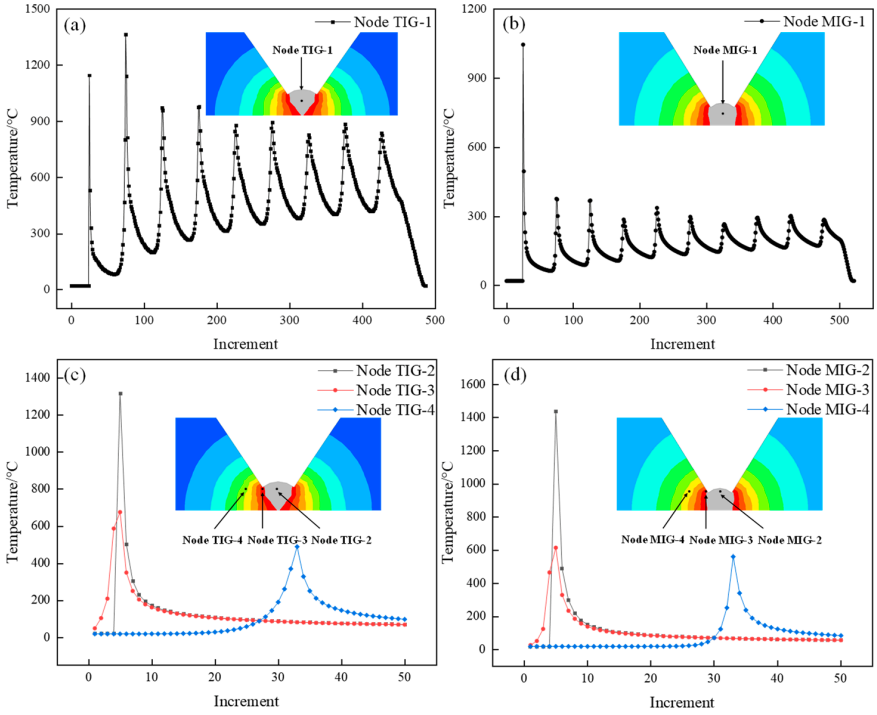


Figure 10. Thermal cycling curves at different nodes: (**a**) overall welding process in TIG welding; (**b**) overall welding process in MIG welding; (**c**) backing welding process in TIG welding; (**d**) backing welding process in MIG welding.

3.2. Structure

Figure 11 shows the structure of the TIG welded joint. As shown in Figure 11a, the cross-section of the TIG butt weld joint has a bowl-shaped profile, with a distinct fusion line and no obvious defects in the joint.

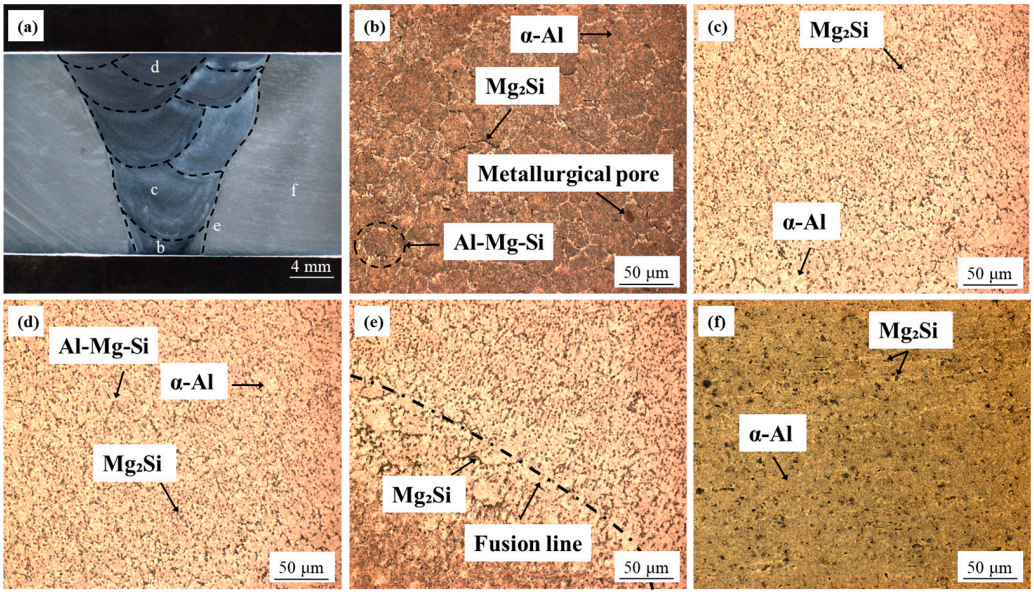


Figure 11. Structure of TIG welded butt joint: (**a**) macrostructure of welded joint; (**b**) microstructure of backing welding in the weld zone; (**c**) microstructure of filling welding in the weld zone; (**d**) microstructure of cosmetic welding in the weld zone; (**e**) microstructure of heat-affected zone; (**f**) microstructure of base metal.

Figure 11b shows that the backing welding forms an α-Al solid solution matrix. Combined with the SEM image in Figure 12a, the granular secondary phase within the grains and at the grain boundaries is a Mg_2Si precipitate. Due to the high heat input and slow cooling rate during backing welding, under continuous thermal cycling, a comparison of Figure 12a,e reveals that the original fine strengthening phases in the base metal have re-dissolved, the precipitated phases exhibit significant overaging behavior, and the Mg_2Si particles have coarsened markedly, which can be confirmed in Table 7. After etching the specimens with Keller's reagent, the more electrochemically active eutectic phases at the grain boundaries and the coarse Mg_2Si phases are preferentially dissolved, forming distinct etching pits under SEM, which clearly reveal the distribution characteristics of the precipitated phases and grain boundaries. Figure 11c reveals that, under repeated thermal cycling, the filling welding exhibits a mixed microstructure of equiaxed and columnar grains. As shown in Figure 12b and Table 7, the grain size of the filler layer has coarsened. Under repeated thermal cycles, the Mg_2Si particles are distributed uniformly within the grains, and the continuous Al-Mg-Si eutectic network at the grain boundaries has gradually fractured, transforming into a discontinuous chain-like structure. Figures 11d and 12c represent the cosmetic welding. The cosmetic welding cools at the fastest rate. Its microstructure consists primarily of equiaxed grains, with the presence of precipitated phases and a chain-like Al-Mg-Si eutectic structure.

A distinct coarsening of the Mg_2Si strengthening phase is observed in the heat-affected zone, as shown in Figures 11e and 12d. Referring to Figures 11f and 12e, the base material consists of a rolled α-Al solid solution, exhibiting distinct rolling grain flow patterns [22]. The structure contains a dispersed network of Mg_2Si aging precipitation phases.

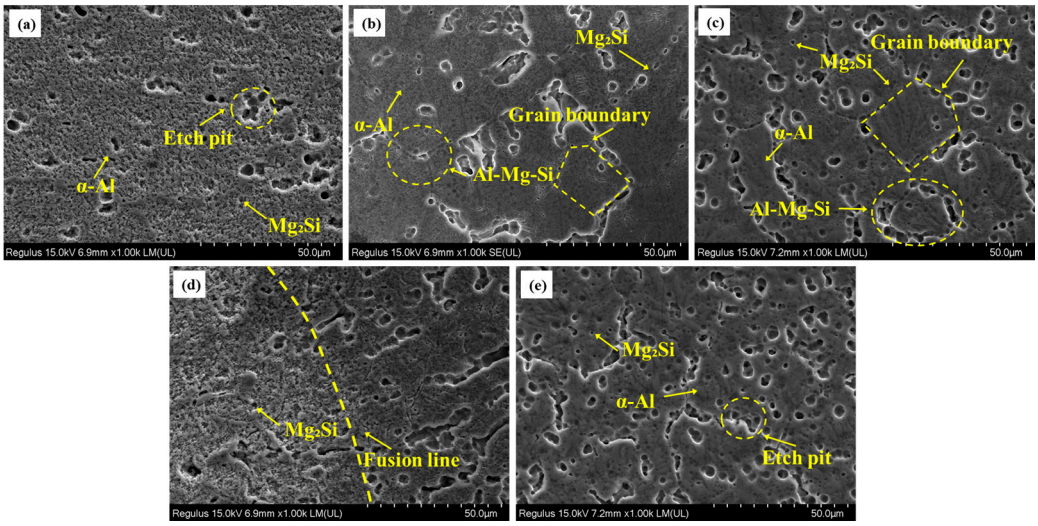


Figure 12. Microstructure of TIG welded butt joint under SEM: (**a**) backing welding in the weld zone; (**b**) filling welding in the weld zone; (**c**) cosmetic welding in the weld zone; (**d**) heat-affected zone; (**e**) base metal.

Table 7. Average grain size of Mg_2Si precipitation phase in different zones (unit: μm).

Welding Process	Backing Welding	Filling Welding	Cosmetic Welding	Heat-Affected Zone	Base Metal
TIG	4.267	4.488	4.307	5.142	3.630
MIG	4.052	3.279	3.106	4.522	3.598

Figure 13 shows the structure of the MIG welded joint. The cross-section of the MIG welded butt joint shown in Figure 13a has a bell-shaped profile, with a more gradual fusion line than that of TIG welding, and the joint shows no obvious defects.

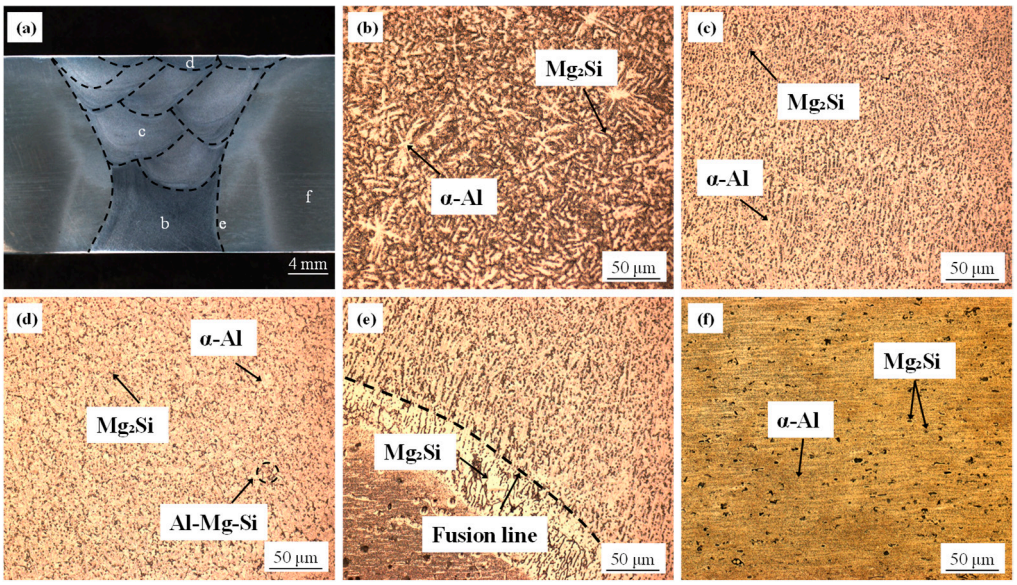


Figure 13. Structure of MIG welded butt joint: (**a**) macrostructure of welded joint; (**b**) microstructure of backing welding in the weld zone; (**c**) microstructure of filling welding in the weld zone; (**d**) microstructure of cosmetic welding in the weld zone; (**e**) microstructure of heat-affected zone; (**f**) microstructure of base metal.

Figure 13b shows the backing welding. Due to poor heat dissipation and the combined effects of thermal cycling, the backing welding exhibits dendritic structures with an α-Al

matrix. Based on the high-magnification SEM morphology shown in Figure 14a, it can be further determined that localized coarsening has occurred in the underlying Mg_2Si precipitation phase [23], which can be confirmed in Table 7. The differences in SEM morphology and corrosion pit size provide clear evidence that the precipitation phase has grown in size and agglomerated locally, resulting in overaging coarsening. However, compared to TIG welding, MIG welding involves more concentrated heat input and faster cooling, so the overall grain structure remains relatively fine. After undergoing multiple thermal cycles, the filling welding develops a microstructure consisting of a mixture of uniform equiaxed grains and residual columnar grains, as shown in Figure 13c. Combined with the high-magnification SEM morphology shown in Figure 14b and average grain size shown in Table 7, it can be further determined that the Mg_2Si precipitation phase exhibits localized coarsening. Some of the previously coarsened precipitation phases have undergone slight resorption and secondary precipitation under repeated thermal cycling, resulting in an increased degree of dispersion of the precipitation phase. Figure 13d shows the microstructure of the cosmetic welding. The cosmetic welding cools most rapidly during welding, which suppresses continued grain growth and ultimately results in the finest equiaxed grain structure within the weld zone.

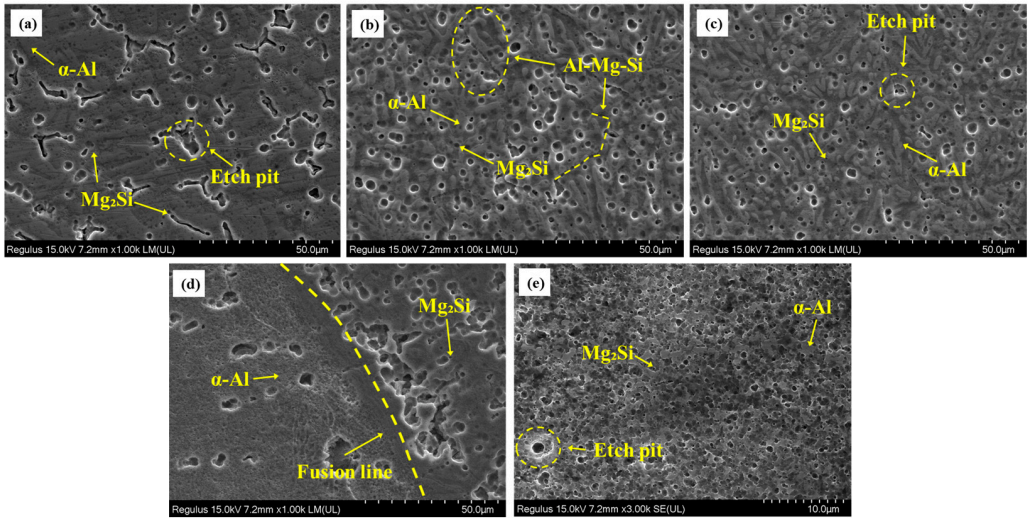


Figure 14. Microstructure of MIG welded butt joint under SEM: (**a**) backing welding in the weld zone; (**b**) filling welding in the weld zone; (**c**) cosmetic welding in the weld zone; (**d**) heat-affected zone; (**e**) base metal.

There is no melting in the heat-affected zone. The Mg_2Si strengthening phases show relatively obvious coarsening, as shown in Figures 13e and 14d. Figures 13f and 14e show the base metal. The matrix consists of an α-Al solid solution and, as with TIG welding, exhibits distinct rolling grain features. The microstructure contains a uniformly distributed Mg_2Si aging precipitation phase, with no evidence of solidification dendrites [24].

Comparing TIG and MIG welds, there are clear differences in their microstructures. The TIG weld has a bowl-shaped profile, a steep fusion line, a coarser overall microstructure, and more pronounced coarsening of precipitation phases. In contrast, the MIG weld has a bell-shaped profile, with a smoother fusion line, a finer and more uniform overall microstructure, and a more dispersed distribution of precipitates. The key reason for the difference lies in the varying heat input and cooling rate of the two welding methods. TIG welding involves high heat input and slow cooling, resulting in a strong cumulative thermal cycling effect that leads to grain coarsening and the aggregation of precipitated phases, thereby degrading performance. MIG welding, with its low heat input, rapid cooling, and minimal thermal cycling effects, promotes grain refinement and the dispersion

of precipitates, thus enhancing material properties. In practical applications, MIG welding demonstrates superior performance in terms of grain refinement and the dispersion of precipitates, providing a more stable microstructural foundation for joint properties. However, due to the microstructural degradation caused by high heat input in TIG single-pass welding, careful control is required during the process.

3.3. Mechanical Properties

3.3.1. Microhardness

Figure 15a shows that the microhardness of the TIG welded butt joint exhibits an M-shaped distribution. The hardness values are highest in the center of the weld, forming a distinct peak. As the heat-affected zone extends outward from the center of the weld, the hardness values gradually decrease and are distributed unevenly. Once the weld reaches the base metal, the hardness is at its lowest and most stable, and the hardness trends of the weld layers are consistent. Figure 15b shows the microhardness of the MIG butt joint. The distribution is relatively uniform, with minimal variation in hardness values across the welds in each layer, and the overall hardness remains at a high level. The hardness transition between the weld zone and the heat-affected zone is smooth, with no obvious peaks or steep drops.

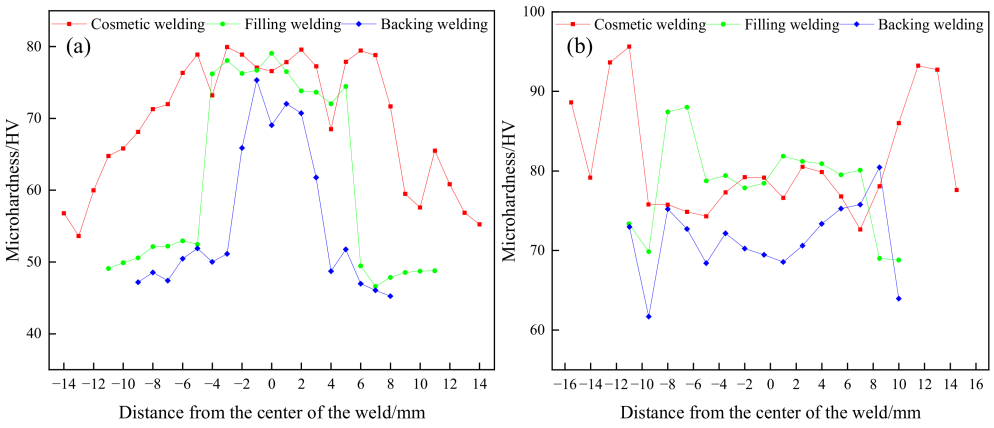


Figure 15. Microhardness distribution of butt joints in the weld zone: (**a**) TIG; (**b**) MIG.

A comparative analysis of microhardness distributions between TIG and MIG welds reveals that heat input and cooling rate have a significant effect on hardness. TIG welding is characterized by high heat input and slow cooling rate. Its concentrated heat source leads to a coarse grain structure in the weld zone. Under slow cooling and prolonged thermal cycling, the Mg_2Si precipitates continuously coarsen, agglomerate and undergo obvious overaging behavior, eventually forming a typical M-shaped hardness distribution. The hardness is relatively high at the weld center and drops sharply in the heat-affected zone due to the obvious coarsening of Mg_2Si precipitates. It demonstrates that the combined effects of coarse grains and overaged, coarsened Mg_2Si precipitates under high heat input cause remarkable hardness fluctuation. MIG welding adopts low heat input and rapid cooling, with a more dispersed heat distribution. The fast cooling process effectively restrains excessive growth of grains and overaging of precipitates inside the weld. Fine equiaxed grains form in each weld layer, and Mg_2Si precipitates maintain a relatively uniform and fine distribution. Partial reprecipitation of precipitates further optimizes the microstructure. Grain refinement strengthening and dispersion strengthening work synergistically. Likewise, the heat-affected zone of MIG welds also shows coarsening of Mg_2Si precipitates under thermal cycling. Different from the M-shaped profile of TIG welds, the hardness distribution of MIG welds is uniform without distinct peaks. This

distribution indicates that fine grains and well-dispersed precipitates in weld metal can improve the hardness stability of welded joints, even though precipitate coarsening occurs in the heat-affected zone of both welding processes [25,26].

Therefore, MIG welding can achieve uniform hardening and deliver optimal performance. Due to microstructural degradation caused by high heat input and slow cooling, TIG welding results in significant variations in hardness and inferior performance. In practical applications, MIG welding is the preferred method, as it allows for the control of grain size and precipitation phases to improve hardness distribution, enhance joint performance, and avoid the low hardness issues associated with the heat-affected zone in TIG welding.

3.3.2. Tensile Properties

Table 8 shows the tensile test results for TIG and MIG butt joints. In terms of TIG welding, the average maximum joint load is 66 kN, and the average tensile strength is 194 MPa. The fracture locations of both sets of specimens are consistently within the heat-affected zone, and the test data shows minimal variation, indicating good consistency in the weak zones of each joint. When it comes to MIG welding, the average maximum joint strength is 86 kN, and the average tensile strength reaches 256 MPa, far exceeding that of TIG welded joints, which can be seen clearly in Figure 16. The fracture locations of both sets of specimens are within the heat-affected zone, and the test data shows no fluctuations, indicating that the microstructure of each joint is uniform and that the weak zones exhibit a high degree of consistency [27].

Table 8. Tensile properties of butt joints in TIG and MIG welding.

Welding Process	Maximum Force/kN	Average Maximum Force/kN	Tensile Strength/MPa	Average Tensile Strength/MPa	Fracture Location
TIG	64	66	193	194	Heat-affected zone
	68		195		Heat-affected zone
MIG	86	86	249	256	Heat-affected zone
	86		263		Heat-affected zone

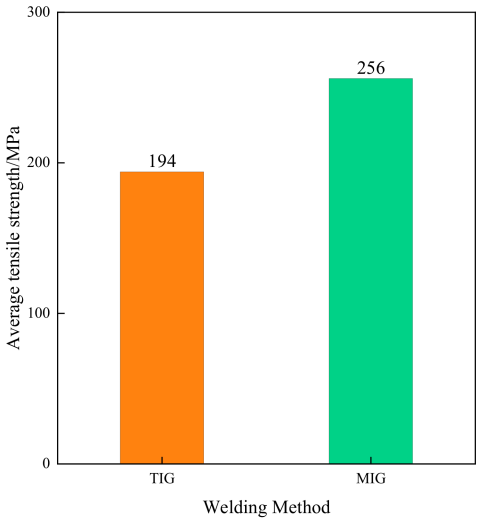


Figure 16. Average tensile strength of welded joints under different welding methods.

Based on the tensile strength data, the tensile strength of MIG welded joints is 32% higher than that of TIG welded joints. The difference in strength between the two is ultimately due to the level of heat input and cooling rate. TIG welding involves high heat

input. Combined with slow cooling, it induces coarsening and aggregation of Mg_2Si precipitates in both the weld zone and heat-affected zone. This microstructural characteristic weakens grain refinement and dispersion strengthening, making the heat-affected zone the weakest link and ultimately resulting in low tensile strength. All tensile specimens fractured within the heat-affected zone, which further verifies that this region is the performance bottleneck of TIG welded joints [28]. In MIG welding, under conditions of low heat input and rapid cooling, fine equiaxed grains form in each weld layer, and the Mg_2Si precipitates are uniformly distributed in a relatively fine, dispersed state. The synergistic effect of fine-grain strengthening and dispersion strengthening significantly enhances the tensile strength. Rapid cooling also restrains grain coarsening in the heat-affected zone and keeps precipitates evenly distributed. Although the heat-affected zone still acts as the fracture location for MIG joints, its overall mechanical performance is much better than that of TIG joints. Therefore, MIG welded joints achieve higher tensile strength. In practical applications, the low heat input MIG welding process should be prioritized to control grain size and precipitation phases, enhance joint strength, and prevent the heat-affected zone from becoming a performance bottleneck. This study only focuses on tensile strength analysis. Fracture morphology characterization and supplementary tensile indicators are not included, which constitutes a limitation of the present work.

3.3.3. Bending Properties

Figure 17 shows the results of bending tests on the TIG and MIG welded butt joint. Neither the TIG welded joint with high heat input nor the MIG welded joint with low heat input fractured during the bending test using a 40 mm diameter mandrel, indicating that the welded joints produced by both processes exhibited good plastic deformation capacity and bending performance.

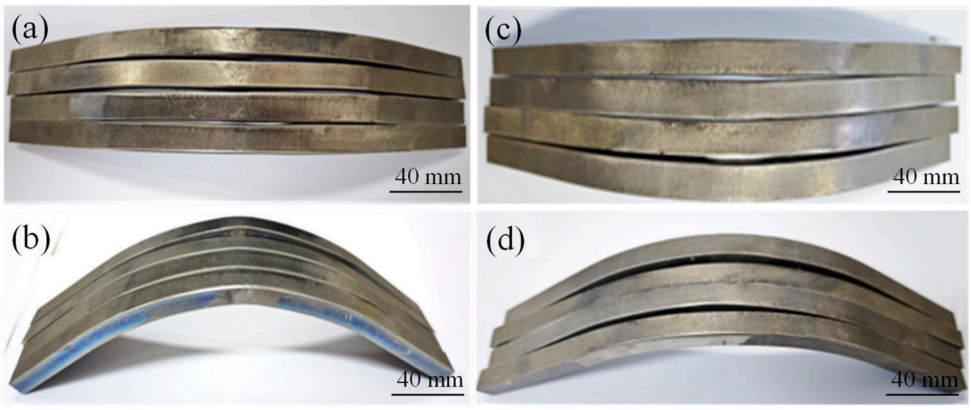


Figure 17. Bending test specimens of butt joints: (**a**) top view of TIG welding; (**b**) front view of TIG welding; (**c**) top view of MIG welding; (**d**) front view of MIG welding.

Although TIG welding introduces high heat input and generates coarse grains within the weld and heat-affected zones, reasonable process parameters can produce sound, dense welds, and the obtained microstructure still possesses plastic deformability. Coarse grains tend to degrade local mechanical performance, while fine grains deliver a strengthening effect. The continuous and compact microstructure enables TIG joints to bear bending loads under the current test conditions [29]. MIG welding applies low heat input with fast cooling rates, forming uniform fine equiaxed grains where Mg_2Si strengthening precipitates are evenly distributed in the Al matrix. Fine grains expand the total grain boundary area [30], hinder dislocation slip and facilitate coordinated plastic deformation. Homogeneously dispersed precipitates restrain crack initiation and maintain stable plastic deformation of the matrix.

A comparison reveals that the differences in bending performance among various welding methods stem from the influence of heat input on the microstructure. When optimized, TIG welding maintains good bending properties through the coordination of a dense microstructure and coarse-grained deformation. MIG welding achieves optimal ductility through fine grains and dispersed precipitates. In practical engineering applications, MIG welding is the preferred method, as it allows for the control of grain size and precipitation phases to enhance bending ductility and meet the requirements for plastic deformation in engineering applications.

Figure 18 reveals the relationship between process, structure, and property. This schematic diagram systematically illustrates the process–structure–property correlation for TIG and MIG welding, showing how welding heat input directly governs temperature field and thermal cycles, which in turn determines the resulting microstructure and final mechanical properties of the joint.

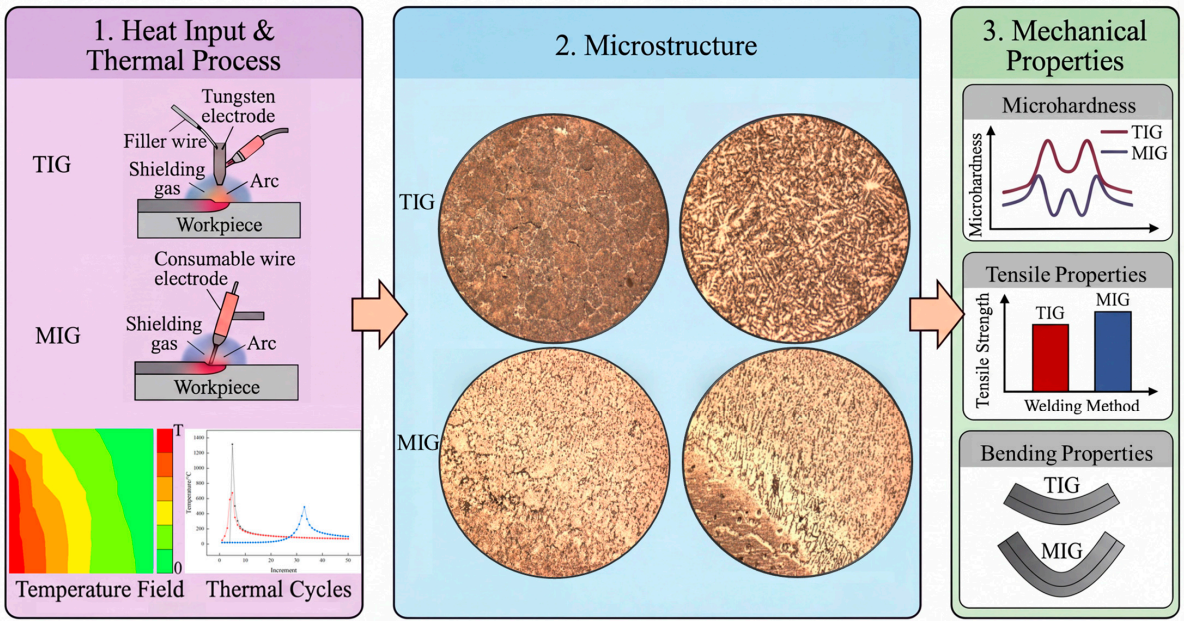


Figure 18. Schematic diagram of the relationship between process, structure, and property.

4. Conclusions

This study primarily investigates the differences in the microstructure, microhardness, tensile properties, and bending properties of 16 mm thick 6082 aluminum alloy subjected to different heat input conditions (high heat input and low cooling in TIG welding and low heat input and fast cooling in MIG welding). The main conclusions are as follows:

- The difference in heat input dominates the thermal distribution of welded joints. TIG welding produces a wide temperature field with steep thermal gradients and severe thermal cycling. In contrast, MIG welding provides concentrated heat input and rapid cooling, forming a uniform temperature field and a regular symmetrical molten pool, which fundamentally reduces thermal structural damage.
- Different thermal conditions lead to distinct microstructural responses. Long-duration high-temperature thermal cycling in TIG welding induces severe coarsening and aggregation of Mg_2Si precipitates, resulting in obvious microstructural degradation. By comparison, the rapid cooling of MIG welding effectively restrains precipitate overaging and excessive growth, thereby obtaining fine grains and uniformly dispersed precipitates with stable microstructure.

- Microstructural differences ultimately determine the mechanical performance of joints. The degraded precipitate strengthening in TIG welds causes uneven hardness distribution and low tensile strength, with the heat-affected zone becoming a structural weak point. Benefiting from the synergistic fine-grain and dispersion strengthening, MIG welded joints achieve stable hardness distribution and exhibit 32% higher tensile strength. Although both welding methods offer satisfactory bending performance, MIG joints possess superior comprehensive mechanical properties and are more suitable for the practical welding of medium-thick 6082 aluminum alloy.

Author Contributions: Conceptualization, Z.J. and S.L.; methodology, F.W. and J.F.; software, Z.J. and S.L.; validation, R.H. and X.X.; formal analysis, F.W.; investigation, J.F.; resources, F.W.; data curation, S.L.; writing—original draft preparation, Z.J. and S.L.; writing—review and editing, F.W. and J.F.; supervision, R.H. and X.X.; project administration, F.W.; funding acquisition, F.W. All authors have read and agreed to the published version of the manuscript.

Funding: This research was funded by the Industry-Academia-Research Collaborative Seed Funding Project of Zhangjiagang City (Grants No. ZKCY2535) and the Technology Development Project of Chinese Ship Scientific Research Center.

Institutional Review Board Statement: Not applicable.

Informed Consent Statement: Not applicable.

Data Availability Statement: The data presented in this study are available on request from the corresponding authors. The data are not publicly available.

Conflicts of Interest: The authors declare no conflicts of interest.

Abbreviations

The following abbreviations are used in this manuscript:

TIG	Tungsten inert gas
MIG	Metal inert gas
SEM	Scanning electron microscope

References

1. Wu, Y.; Kong, L.; Zhang, Y.Q.; Hu, G.F.; Li, Z.H.; He, W.W.; Xue, B.C.; Li, R.S.; Zhang, Y.Z. Comparative analysis and future perspectives on quality inspection of aluminum alloy welds. *Int. J. Adv. Manuf. Technol.* **2026**, *143*, 1281–1310. [CrossRef]
2. Xu, S.X.; Chen, J.X.; Shen, W.; Hou, R.J.; Wu, Y.G. Fatigue strength evaluation of 5059 aluminum alloy welded joints considering welding deformation and residual stress. *Int. J. Fatigue* **2022**, *162*, 106988. [CrossRef]
3. Victor Christy, J.; Ismail Mourad, A.H.; Sherif, M.M.; Shivamurthy, B. Review of recent trends in friction stir welding process of aluminum alloys and aluminum metal matrix composites. *Trans. Nonferrous Met. Soc. China* **2021**, *31*, 3281–3309. [CrossRef]
4. Mohammed, G.R.; Ishak, M.; Aqida, S.N.; Abdulhadi, H.A. Effects of heat input on microstructure, corrosion and mechanical characteristics of welded austenitic and duplex stainless steels: A review. *Metals* **2017**, *7*, 39. [CrossRef]
5. Zhang, X.H.; Chen, J.Q.; Zhang, K.; Chen, H. The softening effect of heat-treated strengthened Al-Zn-Mg alloy in welding process. *Int. J. Mod. Phys. B* **2017**, *31*, 1744039. [CrossRef]
6. Dunder, M.; Samardzic, I.; Simunovic, G.; Konjatic, P. Steel Weldability Investigation by Single and Double-Pass Weld Thermal Cycle Simulation. *Int. J. Simul. Model.* **2020**, *19*, 209–218. [CrossRef]
7. Abbasi, M.; Abdollahzadeh, A.; Bagheri, B.; Moghaddam, A.O.; Sharifi, F.; Dadaei, M. Study on the effect of the welding environment on the dynamic recrystallization phenomenon and residual stresses during the friction stir welding process of aluminum alloy. *Proc. Inst. Mech. Eng. Part L J. Mater. Des. Appl.* **2021**, *235*, 1809–1826. [CrossRef]
8. Oladimeji, O.O.; Taban, E. Trend and innovations in laser beam welding of wrought aluminum alloys. *Weld. World* **2016**, *60*, 415–457. [CrossRef]
9. Chen, C.; Fan, C.L.; Lin, S.B.; Cai, X.Y.; Zhou, L.; Ye, S.F.; Yang, C.L. Effect of ultrasonic pattern on weld appearance and droplet transfer in ultrasonic assisted MIG welding process. *J. Manuf. Process.* **2018**, *35*, 368–372. [CrossRef]

10. Fracchia, E.; Bidulska, J.; Bidulsky, R.; Actis Grande, M. MIG and TIG joining of AA1070 aluminium sheets with different surface preparations. *Materials* **2022**, *15*, 412. [CrossRef] [PubMed]
11. Rojas, H.; Molina, A.; Valdez, S.; Campillo, B.; Martínez, H.; Sedano, A.; Serna, S. The impact of heat input on the microstructures, fatigue behaviors, and stress lives of TIG-welded 6061-T6 alloy joints. *Mater. Res. Express* **2020**, *7*, 126512. [CrossRef]
12. Cheng, Z.; Ye, Z.; Huang, J.H.; Yang, J.; Chen, S.H.; Zhao, X.K. Influence of heat input on the intermetallic compound characteristics and fracture mechanisms of titanium-stainless steel MIG-TIG double-sided arc welding joints. *Intermetallics* **2020**, *127*, 106973. [CrossRef]
13. Wang, T.H.; Li, Y.W.; Mao, Y.H.; Liu, H.F.; Babkin, A.; Chang, Y.L. Research status of deep penetration welding of medium-thick plate aluminum alloy. *Int. J. Adv. Manuf. Technol.* **2022**, *120*, 6993–7010. [CrossRef]
14. Chen, Y.X.; Xu, X.; Liu, Y.J.; Cui, H.C. A comparative study on microstructural characterization of thick high strength low alloy steel weld by arc welding and laser welding. *Materials* **2023**, *16*, 2212. [CrossRef] [PubMed]
15. Ye, Z.; Huang, J.H.; Cheng, Z.; Gao, W.; Zhang, Y.F.; Chen, S.H.; Yang, J. Combined effects of MIG and TIG arcs on weld appearance and interface properties in Al/steel double-sided butt welding-brazing. *J. Mater. Process. Technol.* **2017**, *250*, 25–34. [CrossRef]
16. Qin, B.; Qu, R.; Xie, Y.F.; Liu, S. Numerical Simulation and Experimental Study on the TIG (A-TIG) Welding of Dissimilar Magnesium Alloys. *Materials* **2022**, *15*, 4922. [CrossRef] [PubMed]
17. Larsen, M.L.; Arora, V.; Lützen, M.; Pedersen, R.R.; Putnam, E. Fatigue life estimation of the weld joint in K-node of the offshore jacket structure using stochastic finite element analysis. *Mar. Struct.* **2021**, *78*, 103020. [CrossRef]
18. Doshi, S.; Jani, D.B.; Gohil, A.V.; Patel, C.M. Investigations of heat source models in transient thermal simulation of pulsed MIG welding of AA6061-T6 thin sheet. *IOP Conf. Ser. Mater. Sci. Eng.* **2021**, *1146*, 012015. [CrossRef]
19. Hu, Y.; Pei, W.C.; Ji, H.C.; Yu, R.D.; Liu, S.Q. Tungsten inert gas welding of 6061-T6 aluminum alloy frame: Finite element simulation and experiment. *Materials* **2024**, *17*, 1039. [CrossRef] [PubMed]
20. Jeon, J.Y.; Oh, C.Y.; Kim, C.K. Analysis of variables in finite element analysis for multi-pass welding in nuclear power plant components, part 1: Comprehensive study with experimental validation using scientific weld specimen. *Nucl. Eng. Technol.* **2025**, *57*, 103275. [CrossRef]
21. Wang, H.; Yang, X.J.; Madeniyeti, N.; Qiu, J.; Zhu, C.H.; Yin, L.; Liu, K.F. Temperature Distribution of Vessel Tissue by High Frequency Electric Welding with Combination Optical Measure and Simulation. *Biosensors* **2022**, *12*, 209. [CrossRef] [PubMed]
22. Gadallah, E.A.; Abd El Aal, M.I.; Mohamed, A.Y.; El-Fahhar, H.H. Effects of filler on the microstructure and corrosion of similar and dissimilar gas inert tungsten arc welding aluminum alloys joints. *Sci. Rep.* **2023**, *13*, 19011. [CrossRef] [PubMed]
23. Naing, T.H.; Muangjunburee, P. Metallurgical and mechanical characterization of MIG welded repair joints for 6082-T6 aluminum alloy with ER 4043 and ER 5356. *Trans. Indian Inst. Met.* **2022**, *75*, 1583–1593. [CrossRef]
24. Wang, W.H.; Gu, X.P.; Shao, J.X.; Gu, X.Y.; Zhu, L.J. Effect of current waveform characteristics on the double-pulse metal inert gas welded joint for 6082 aluminum alloy. *J. Mater. Eng. Perform.* **2025**, *34*, 29756–29771. [CrossRef]
25. Xu, X.H.; Li, X.F.; Zhai, W.G.; Zhou, W. Laser-tungsten inert gas (TIG) hybrid welding of a 5052 aluminum alloy, part B: Microhardness and tensile strength analysis. *Laser Eng.* **2017**, *37*, 169–175.
26. Baskutis, S.; Zunda, A.; Kreivaitis, R. Mechanical properties and microstructure of aluminium alloy AW6082-T6 joints welded by double-sided MIG process before and after aging. *Mechanika* **2019**, *25*, 107–113. [CrossRef]
27. Ma, C.P.; Kang, G.Z.; Gou, G.Q.; Chen, H.; Che, X.L. Effect of charging hydrogen on the tensile properties of A7N01 aluminum alloy friction stir welded joints. *Int. J. Mod. Phys. B* **2019**, *33*, 1940043. [CrossRef]
28. Liu, H.B.; Gu, A.; Chen, Z.H.; Tan, Z.L.; Zhou, G.G. Mechanical properties and design method of aluminum alloy bolt-sphere joints. *Struct. Eng. Int.* **2021**, *31*, 30–39.
29. Kaboglu, C.; Mohagheghian, I.; Zhou, J.; Guan, Z.W.; Cantwell, W.; John, S.; Blackman, B.R.K.; Kinloch, A.J.; Dear, J.P. High-velocity impact deformation and perforation of fibre metal laminates. *J. Mater. Sci.* **2018**, *53*, 4209–4228. [CrossRef]
30. Bin Ali, S.; Kamaris, G.S.; Gkantou, M. Flexural behaviour of concrete-filled double skin aluminium alloy tubes. *Eng. Struct.* **2022**, *272*, 114972. [CrossRef]

Disclaimer/Publisher's Note: The statements, opinions and data contained in all publications are solely those of the individual author(s) and contributor(s) and not of MDPI and/or the editor(s). MDPI and/or the editor(s) disclaim responsibility for any injury to people or property resulting from any ideas, methods, instructions or products referred to in the content.